Journal of Nonlinear Optical Physics & Materials
Vol. 15, No. 2 (2006) 203-218

World Scientific
www.worldscientific.com

LUMINESCENT AND TUNABLE 3D PHOTONIC CRYSTAL STRUCTURES

C. J. SUMMERS, E. GRAUGNARD, D. P. GAILLOT and J. S. KING

School of Materials Science and Engineering
Georgia Institute of Technology
Atlanta, Georgia 30332-0245
chris.summers@mse.gatech.edu

Received 28 April 2006

We report an investigation of luminescent and tunable photonic crystal structures formed by the infiltration and inversion of opal templates with high index and luminescent materials. Protocols are reported for the deposition of these materials and the properties of the resulting structures investigated by conventional structural and optical measurements. The properties of multi-layered and backfilled structures are reported and demonstrate the potential to modulate and statically tune the luminescence from photonic crystals.

Keywords: Colloidal photonic crystals; atomic layer deposition; photoluminescence; TiO_2; ZnS

1. Introduction

Three-dimensional photonic crystals are being actively investigated because of their potential for controlling light with a precision hitherto not possible.[1, 2] Dielectric doping to create a luminescent defect state, or microcavity, within the band gap of a photonic crystal enables the spontaneous emission properties, (intensity, threshold and emission energy) to be manipulated,[3] so as to achieve very narrow line widths, high luminosity and potentially, spectral tunability by the incorporation of liquid crystals.[4] To realize these properties ideally requires a large full photonic band gap (PBG) which can be achieved by the use of high index materials[5] and low symmetry structures,[6] as predicted theoretically for diamond-like lattices ($n > 1.9$)[7] and demonstrated by the silicon log-pile structure in the infrared.[8] However, simpler structures can be manufactured by a "bottom-up" self-assembly approach based on opal technology,[9-11] although in this case only a directionally-dependent pseudo PBG (PPBG) will be formed.[5] Fortunately, this is along the (111) direction which is also the preferred assembly direction.[12] Additionally, the placement of the dielectric material in the structure is very important, and for obtaining both luminescent and tunable properties, the integration of different classes of materials is crucial.

In this paper we present the progress made to develop luminescent 3D PCs based on the exploitation of new crystal structures derived from the fcc lattice, coupled with the infiltration of high index and luminescent materials by atomic layer deposition (ALD). We show that effective structures can be

made by this technique and offer considerable flexibility in examining new concepts (such as a photonic crystal phosphor) as well as serving as test beds for developing the growth/fabrication tools for their construction. Additionally, to achieve these properties in the visible requires the incorporation of optically transparent materials, and for light generation, luminescent materials. For example, we have investigated non-close-packed opal (NCP) structures and the use of luminescent material (ZnS:Mn) coupled with higher index material (TiO_2) to form multi-layer combined infiltrations. These structures are still limited as they cannot support a full PBG, due to restrictions of index and geometry, however they provide a very effective way to develop protocols that can be transferred to lower symmetry lithographically-derived structures. The materials investigated were ZnS:Mn, because of its luminescent properties, relatively high index (2.52-2.24 between 400 and 700nm) and transparency in the visible and near infrared; and TiO_2 (anatase phase) because it has a higher refractive index in the visible region (2.9 - 2.5 between 400 and 700 nm) and high transparency.

For these materials the design considerations for multi-layered ZnS:Mn/TiO_2-based inverse opals has been examined. For a multi-layered structure, the dielectric approximation gives the effective refractive index as: $[x_1 n_1^2(\lambda) + x_2 n_2^2(\lambda)]^{1/2}$, where x_k and n_k are the volume fraction and refractive indices of component k. Thus, to support a full PBG in an inverse opal, $[x_1 n_1^2(\lambda) + x_2 n_2^2(\lambda)]^{1/2} \geq 2.8$. At 450 and 400 nm, the refractive indices of ZnS and the rutile phase of TiO_2 are, 2.46 and 2.52, and 3.0 and 3.2, respectively. A ZnS:Mn/TiO_2 multi-layer inverse opal will support a full PBG if the ZnS:Mn content is less than 39% at 450 nm, or 61% at 400 nm. The rutile phase of TiO_2 has proven to be difficult to form, while the anatase phase which forms quite easily, has an index of 2.7 at 450 nm, and 2.9 at 400 nm. At 400 nm, it is thus possible to form a ZnS:Mn/anatase TiO_2 multi-layer with a full PBG if the ZnS:Mn content is less than 27%.

2. Experimental Procedures

2.1. Opal Fabrication

For this study silica opals were formed by self-assembly, as previously reported.[9] Atomic layer deposition was then used to conformally infiltrate the opal templates and the properties of infiltrated and inverted structures (obtained by etching out the original template) were measured.

The growth of ZnS:Mn was performed in a Microchemistry, Ltd. F120 reactor following the normal procedure for this material, but with extended precursor and purge pulse durations of 2 s.[13, 14] Reasonably conformal layers were produced, but exhibited some nanoscale roughness. Thus, for the growth of TiO_2, using a custom-built, flow-style, hot-wall ALD reactor, special protocols were developed to obtain high conformity and optimum crystallinity, and to address the requirements of depositing material within a highly porous structure.[15] The initial studies on the growth of the high index rutile phase of titania on planar substrates showed that even for growth temperatures above 600^o C, it was difficult to reproducibly form the rutile phase and that the resulting polycrystalline films exhibited considerable surface roughness which

increased with deposition temperature.[16] However, as shown by Figure 1, by significantly decreasing the growth temperature (~100 ºC) very low RMS roughness (0.2 nm) films were achieved. X-ray studies showed that these films were amorphous at the lowest deposition temperature, exhibited the anatase phase above 200 ºC and a mixed anatase/rutile phase for growth at 600 ºC.[16] However, by annealing the films deposited at low temperature it was found that they could be converted to the higher index anatase phase while still retaining their smooth conformal growth properties. From this study the following protocol was developed for opal infiltration: initial deposition at 100 ºC followed by annealing at 400-500 ºC for 2 hours. This produced very smooth films of the anatase phase with an index value of about 2.8 at 430 nm. For infiltrations into opal structures the same protocols were used, however the precursor and purge times were increased to 8 and 20 s, respectively. As shown in Figure 2, this procedure produced very uniform TiO_2 inverse opals for depositions within silica opal templates.

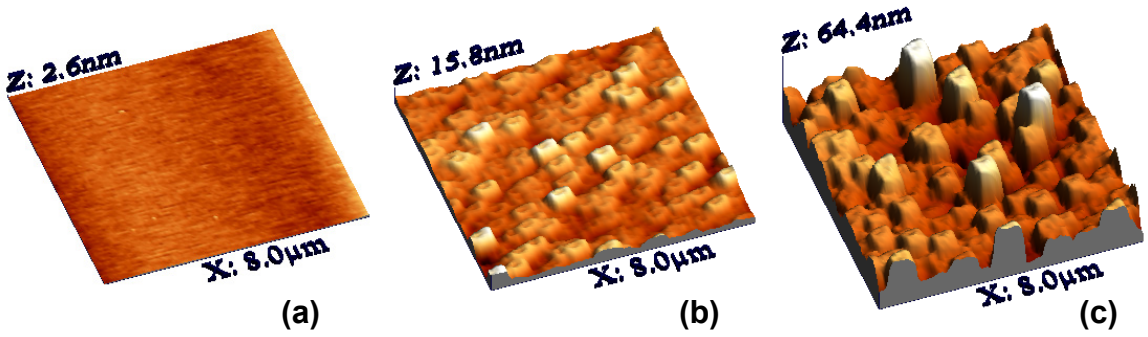

Fig. 1. AFM images of TiO_2 planar films grown by ALD at (a) 100, (b) 300, and (c) 600 ºC. RMS roughness values of 0.2, 2.1, and 9.6 nm were measured, respectively.

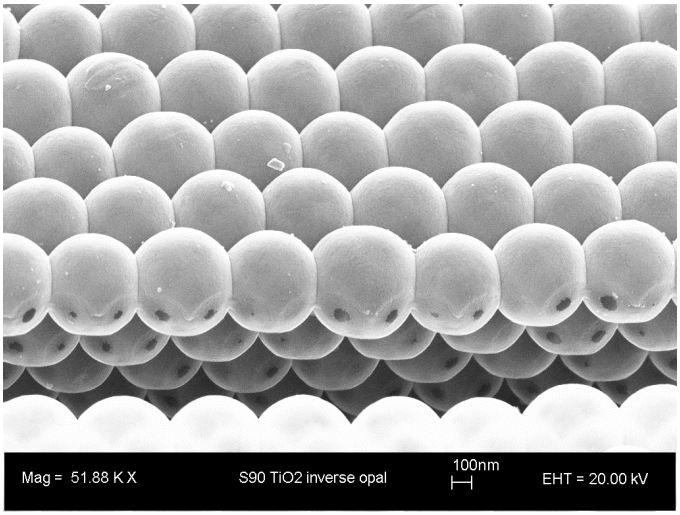

Fig. 2. TiO_2 inverse opal grown by 100 ºC ALD infiltration of a 466 nm SiO_2 opal, followed by a 400 ºC, 2 hr. heat treatment and HF etching.

2.2. Structural Characterization

The structural properties of the resulting films were examined by SEM. Figure 3 shows an ion-milled cross-section of the (111) plane of a ZnS:Mn/TiO_2/air inverse opal, clearly revealing the resulting periodic structure of high dielectric material and air spheres. This structure was formed by infiltrating an opal comprised of 330 nm silica spheres with a 10 nm layer of TiO_2, followed by a 10 nm layer of ZnS:Mn. The top layers were next ion milled, exposing the silica spheres, and enabling their removal using a 2% HF solution. The maximum thickness for conformally infiltrated material for this opal size is 25.6 nm, so as expected, there is still some air remaining in the original pore volume, as confirmed by the dark regions adjacent to the ZnS:Mn layer in the figure. Closer examination of the image clearly revealed two distinct conformal layers that comprise the structure, with the TiO_2 layer being the first layer (closest to the "air sphere") and the second being the ZnS:Mn layer. The larger dark spots on the surface of the air spheres are the air holes resulting from the connectivity between the SiO_2 spheres formed after sintering and prior to infiltration. The inset shows a higher magnification of the multi-layer region formed at the interstice between the air spheres. In this image, the darker material is TiO_2 and the lighter material ZnS:Mn, again with the darkest region being air due to intentional incomplete infiltration.

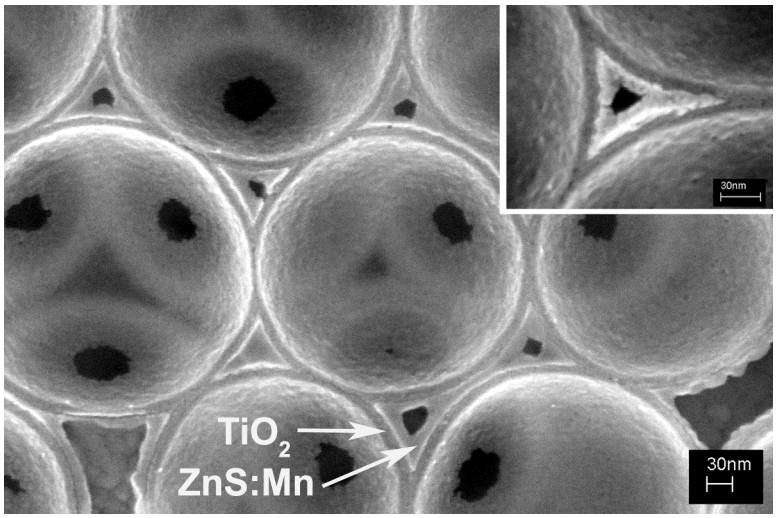

Figure 3. ZnS:Mn (10 nm)/TiO_2 (10 nm) opal photonic crystal formed by the infiltration/inversion of a 330 nm silica opal. Insert shows detail of multi-layer region.

Figure 4 shows a similar SEM cross section of a TiO_2/ZnS:Mn/TiO_2/air (24/10/10 nm) inverse opal, where the original sphere diameter was 433 nm. This photonic crystal was fabricated in a similar manner, but the first infiltrated layer was ZnS:Mn, and after removing the silica spheres, a second layer of TiO_2 was deposited on the interior surface of the 2-layer inverse opal. The inset depicts the resulting three-layer inverse structure prior to the final ion milling step. The layers are labeled in the image, where the TiO_2 layers are the gray regions, and the ZnS:Mn layer is the lighter region sandwiched between them.

Clearly the layers are highly conformal and spatially distinct, and indicate the successful formation of a multi-layer inverse opal.

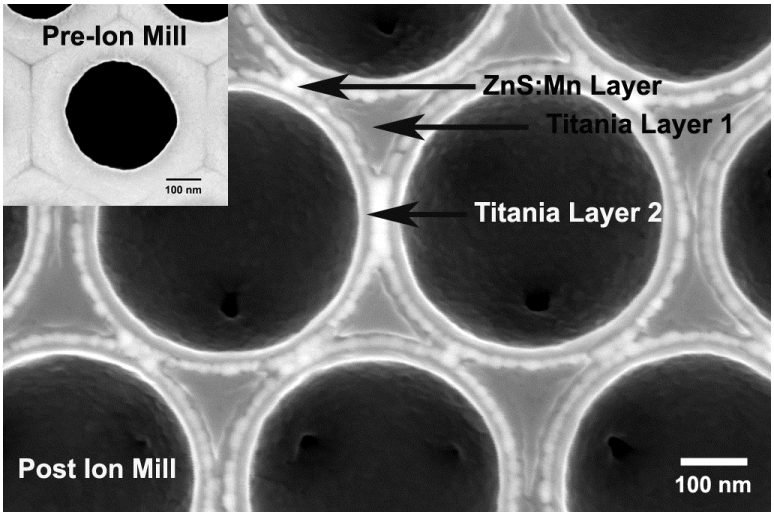

Fig. 4. Three-layer, backfilled TiO_2/ZnS:Mn/TiO_2 inverse opal. Inset shows surface prior to 2nd ion mill step.

2.3. X-ray Diffraction Studies

X-ray studies were performed to assess the crystallinity of the infiltrated materials, and for confirmation of the conversion of the amorphous as-deposited TiO_2 layers to the crystalline phase. As shown in Figure 5(i), X-ray diffraction measurements on a ZnS:Mn infiltrated opal confirm the wurtzite phase for the deposition conditions of 450 ºC for an 8 hr run. Figure 5(ii) confirms the transformation of infiltrated TiO_2, deposited at 100 ºC for 8 hrs, from the amorphous to the crystalline anatase phase after a 2 hr anneal at 400 ºC.

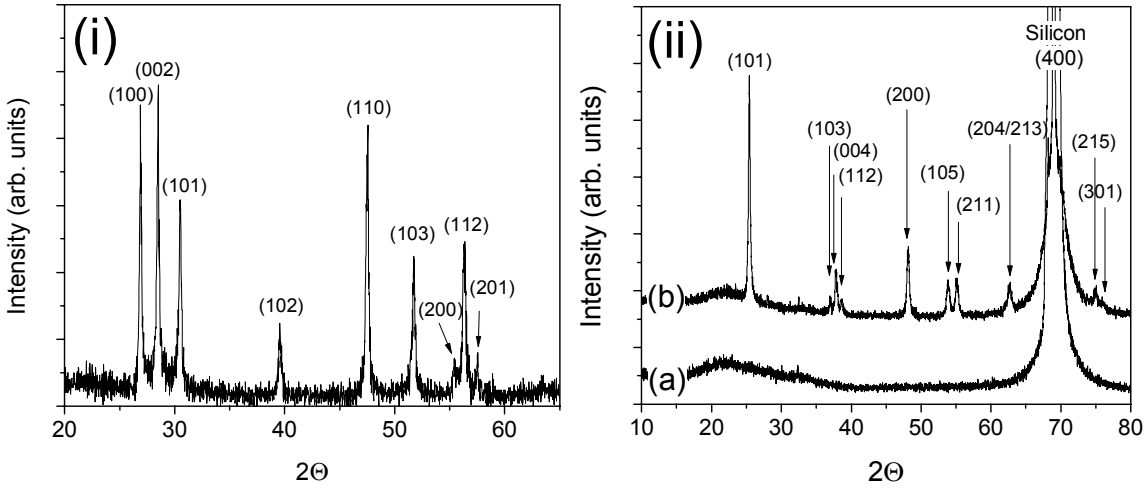

Fig. 5. (i) X-ray diffraction data for a ZnS:Mn infiltrated opal, and (ii) for an (a) amorphous TiO_2 infiltrated opal, and (b) after 400 ºC, 2 hr. heat treatment, yielding the crystalline anatase phase.

The presence of both TiO_2 and ZnS:Mn in the multi-layer structure was also confirmed, as shown in Figure 6. This figure clearly shows the existence of peaks from both infiltrated materials, labeled "A" or "W", to denote the anatase or wurtzite phase, respectively, and indexed with the respective planes responsible for diffraction. The broad hump-like peak starting at $2\theta = 20°$ and extending to $\sim 2\theta = 32°$ is characteristic of amorphous materials, and is therefore attributed to the silica spheres comprising the opal template.

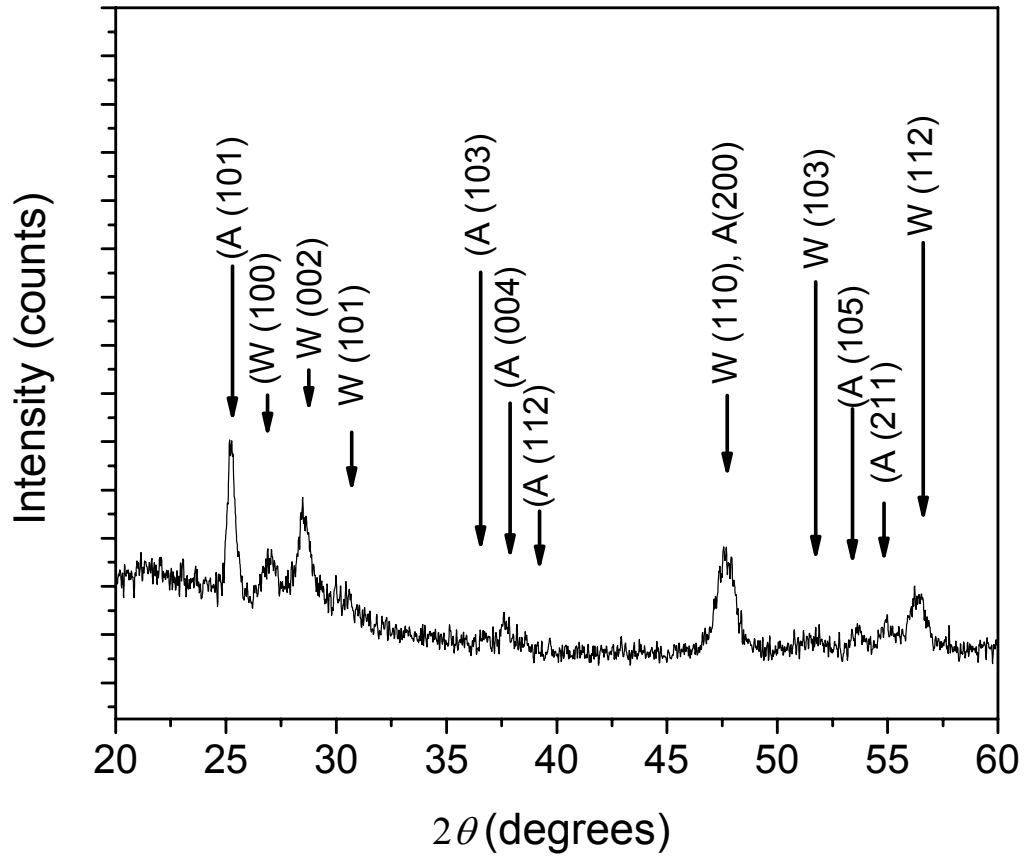

Fig. 6. X-ray diffraction data for a ZnS:Mn + TiO_2 multi-layered infiltration of a silica opal. TiO_2 reflections are indicated by A(ijk), and ZnS:Mn by W(ijk).

2.4. Optical Characterization

During fabrication, the effect of each processing step was followed by examining the wavelength shift of the primary Γ-L PPBG peak in the specular reflectance. This peak is due to Bragg diffraction from the (111) planes, and corresponds to the PPBG formed between the 2nd and 3rd photonic bands. In opal-based PCs, the PPBG widens as the refractive index contrast increases. Figure 7 plots the reflection spectra, measured at 15° from normal incidence, during the formation of a three-layer inverse opal based on a 330 nm SiO_2 opal template. For this sample, the opal template was first infiltrated with 10 nm of ZnS:Mn,

followed by 7.5 nm of TiO_2 (a summed partial infiltration of ~ 17.5 nm). After removal of the SiO_2 spheres, the inverse opal was backfilled with 10 nm of TiO_2. The peaks were centered at 714 nm for the sintered opal (curve a), 822 nm after infiltration with 10 nm of ZnS:Mn (curve b), and 866 nm after 7.5 nm of TiO_2 (curve c). Using Bragg's law, these peak positions indicate average dielectric constants (ε_{avg}) of 1.81, 2.38, and 2.63, for the SiO_2, SiO_2/ZnS:Mn, and SiO_2/ZnS:Mn/TiO_2 composites, respectively. After removing the SiO_2 spheres, thus forming a 2-layer inverse opal, the peak shifted to 721 nm (curve d), indicating a decrease in ε_{avg} to 1.84. Backfilling the air voids with ~ 10 nm of TiO_2 shifted the Γ-L PPBG peak to 877 nm (curve e), a longer wavelength than the peak position for the 2-layer infiltrated opal, indicating an increase in ε_{avg} to 2.63. This confirmed that backfilling with a relatively small amount of TiO_2 significantly impacts the optical properties, and thus the photonic band structure of the PC. The broad reflectivity peaks for the 2- and 3-layer inverse opals (curves d and e) at ~ 380 and 480 nm, respectively, are attributed to Γ-L PPBGs that form between the 5th and 6th and the 8th and 9th bands in a single component inverse opal, as calculated using the plane wave expansion method.

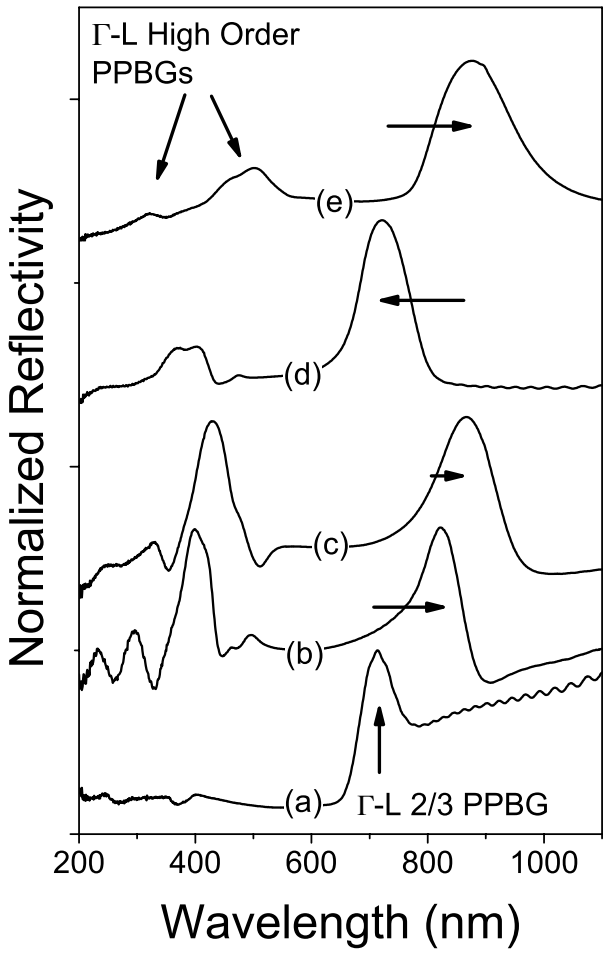

Fig. 7. Reflectivity spectra for 330 nm (a) sintered SiO_2 opal, (b) ZnS:Mn (10 nm) infiltrated opal, (c) ZnS:Mn/TiO_2 (10/7.5 nm) infiltrated opal, (d) ZnS:Mn/TiO_2 inverse opal, and (e) TiO_2/ZnS:Mn/TiO_2 (10/10/7.5 nm) inverse opal. (15° from normal)

A similar study is shown in Figure 8 for a 433 nm sphere diameter based opal, where the results are compared to theoretical calculations. The Γ-L section of the photonic band diagram for the two-layer multi-layered opal consisting of a 24 nm TiO_2 layer and a 10 nm ZnS:Mn layer was calculated using the effective index approximation for the refractive index used in the simulation, instead of creating a dielectric function with distinct layers of differing refractive index. This band diagram is shown in Figure 8(a), as compared to the measured reflectivity data. Two wide and a narrow PPBG were predicted in the high energy portion of the band diagram, between the 5^{th} and 6^{th}, 8^{th} and 9^{th}, and the 10^{th} and 11^{th} bands. The peak in the reflectivity matches the position of the gap between the 5^{th} and 6^{th} bands. While there is no other distinct peak in the reflectivity, the width of the peak spans the width of the three band gaps. The PPBG between the 2^{nd} and 3^{rd} bands is located in the long wavelength region on the diagram, and is wide, in agreement with the reflectivity peak in both position and width.

The same portion of the band diagram was recalculated after backfilling with 5 nm of TiO_2 and compared with the measured reflectivity data, as shown in Figure 8(b). The primary peak shifted partially beyond the measurement range, such that the long wavelength band edge could not be measured from the reflectivity data, but the peak position agrees with the band diagram. The band diagram indicates that by slightly backfilling the inverse opal, the same band gaps are present as before, but the 10^{th} to 11^{th} gap has opened wider, and another gap has opened between the 12^{th} and 13^{th} bands. The high energy reflectivity peak again spans the wavelength range of these 4 band gaps.

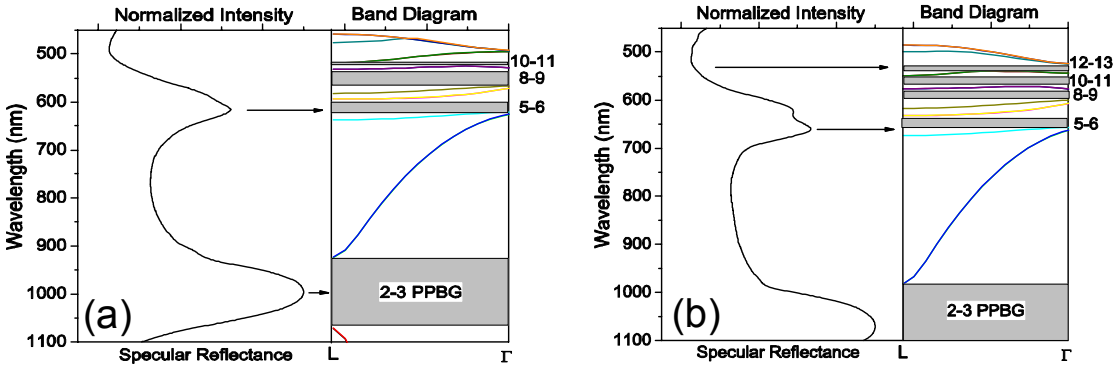

Fig. 8. Specular reflectivity compared with the photonic band diagram for (a) a two-layer 433 nm inverse opal, TiO_2/ZnS:Mn (24/10 nm) and (b) after backfilling with 5 nm of TiO_2. (15 degrees)

2.5. Photoluminescence Study

The photoluminescence (PL) response of the structures described in Figure 8 were measured using 45º incident 337 nm pulsed UV excitation. The PL was collected normal to the (111) surface after each backfilling step of the 3-layer inverse opal as shown in Figure 9. The corresponding reflectivity data is included for comparison. Emission peaks were observed at both 460 nm and 585 nm, corresponding to Cl^- defect donor-acceptor and Mn^{2+} luminescent center emission, respectively. The 585 nm emission peak is coincident with the high order PPBGs found in the TiO_2/ZnS:Mn inverse opal. When the curves were normalized to the 460 nm peak, a systematic increase in the PL intensity was observed. For the 585 nm

peak as the PBGs shifted (off the Mn^{2+} emission peak) to longer wavelengths, a 108% increase in the PL intensity was observed with increasing TiO_2 backfilling. The increase in PL intensity is thus attributed to the shifting of the high order band gap off the 585 nm peak, and/or the emission enhancement expected at the photonic band edge.

Thus, this study demonstrated that both luminescent ZnS:Mn inverse opals and also multi-layer inverse opals could be fabricated by the ALD of ZnS:Mn and TiO_2, thereby demonstrating independent control of refractive index and modification of luminescence with high-order photonic bands. However, despite the 2X tuning of the luminescence intensity from a multi-layer PCP, this structure still does not exhibit a full photonic band gap, and there remains a need for new structures and geometries for improved and tunable devices.

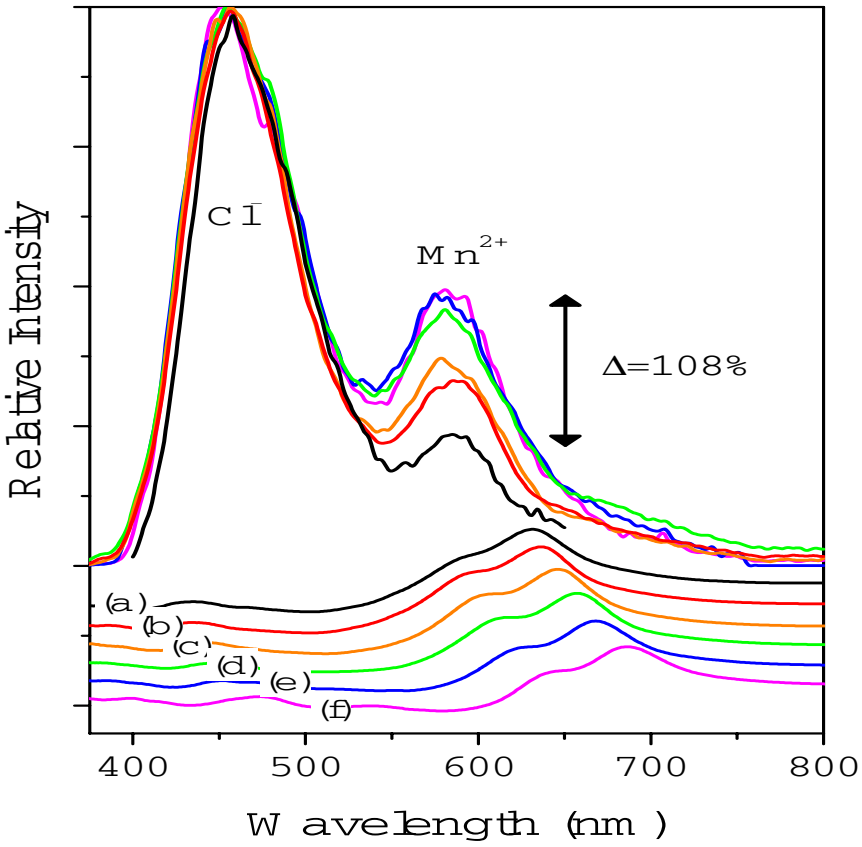

Fig. 9. Photoluminescence (upper curves) compared with specular reflectivity (lower curves) as measured for (a, black) TiO_2 (14 nm)/ ZnS:Mn (20 nm)/air 433 nm inverse opal and after backfilling with (b, red)) 1 (c, orange) 2, (d, green) 3, (e, blue) 4, and (f, magenta) 5 nm of TiO_2.

2.6. Non-Close-Packed Inverse Opals

Recent theoretical work has shown that in non-close-packed inverse opals the PBG can be increased by a factor of two, to ~11% of the average gap wavelength, and that directionally dependent pseudo-photonic band gaps (PPBGs) can be very effective in providing the capability for dielectric doping

and consequently control over emission. Thus, the development of these structures is expected to have significant advantages.

In non-close-packed geometries formed by sintering,[17] the periodicity is reduced by collapsing the interlocking network of spheres and the structure becomes a collection of dumb-bell connections as shown in Fig. 10. However, now two parameters define the geometry, the normalized radii of the air spheres, R_s/a, and the connecting air cylinders, R_c/a, respectively, where a is the cubic lattice constant of the collapsed structure. Simulations show that both R_s and R_c have a strong effect on the gap width and can lead to a reduced refractive index requirement to form a PBG.[18] As shown by Figure 10, practically, these structures result from a combination of heavy sintering (that collapse the silica spheres) and conformal infiltrations after removal of the template. The heavy sintering treatment controls the dielectric/air backbone, and the backfilling infiltration the "peanut-like" connections between the air spheres of the NCP lattice. Simulations of these structures predict gap widths as high as 7.5% for Si and a reduced refractive index contrast requirement for opening a PBG of n~2.7.[18]

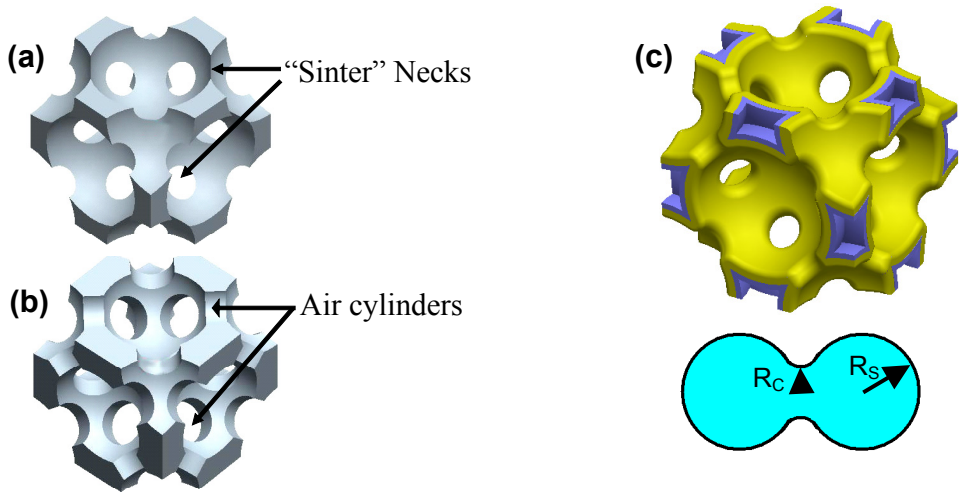

Fig. 10. Comparison between simple inverse opal (a) and NCP inverse opal structures (b). (c) Schematic of a conformally filled NCP structure and the resulting "peanut" connection between adjacent air spheres.

As shown by Figure 11(a), sintering an opal prior to infiltration increases the neck-diameter between spheres such that after infiltration the pores become larger. For the example shown, the opal was infiltrated with TiO_2 and then etched in HF to remove the SiO_2 spheres to form a large-pore inverse opal. Back-filling with TiO_2 created air cylinder connections, as shown in Figure 11(b) which shows a TiO_2 NCP inverse opal, formed from a heavily sintered 460 nm SiO_2 opal after 700 TiO_2 ALD backfilling cycles.

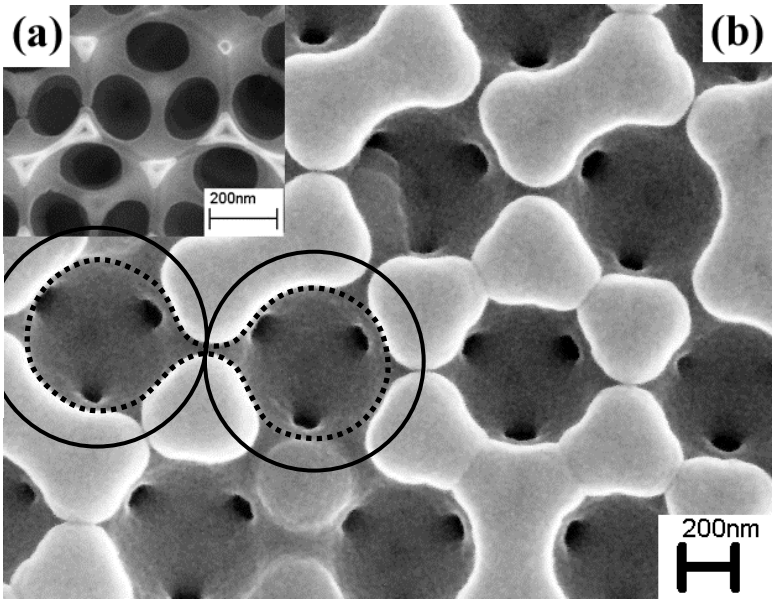

Fig. 11. Large-pore inverse opal (a) and non-close-packed inverse opal (b) after backfilling with 700 TiO_2 ALD cycles (36 nm). The solid and dotted construction lines show the original sphere diameters and the dumbbell arrangement, respectively, that results from sintering and backfilling.

In fact the resulting inverse opal was infiltrated with amorphous TiO_2 in steps of 40 ALD cycles, to a total of 700. From our previous work, an opal infiltration growth rate of 0.51 Å/cycle was used to estimate the thicknesses of the infiltrated TiO_2.[15] The evolution of the reflectivity spectra during formation of the non-close-packed structure is shown in Figures 13 and 14, after 160, 280, 400, and 520 ALD cycles. The data for the NCP inverse opal is also shown for clarity. Figure 12 and 14 cover the wavelength range that includes the Bragg peak and higher energy regions comprising the flat band and higher order PPBG peaks, respectively. Both figures include the relevant portions of the corresponding Γ-L photonic band diagrams for each structure, as calculated using the FDTD method. Because of the normal dispersive properties of TiO_2, its refractive index varies significantly for different wavelengths; thus two sets of calculations were performed for each structure, using the appropriate refractive indices, n_{an} and n_{am}, for the anatase and amorphous phases, respectively. As shown in Figure 12, excellent agreement was found between the experimental reflectivity data and the theoretical predictions of the photonic band structure, ranging from the NCP opal to very high levels of conformal infiltration. As observed, both the position and width of the reflectivity peak progressively increase from 739 nm to 1039 nm and, 60 nm to 125 nm, respectively, with increasing conformal depositions of titania, i.e. increasing mass of dielectric material. When calculating the photonic band structures a "conformal" model was used for the generation of the required dielectric functions, which exactly simulates the ALD growth topography. This produces a dielectric function that faithfully replicates the real structure by taking into account the actual shapes of the air spheres, and the connecting regions between them that result after conformal backfilling. The resulting band diagrams were then calculated using the finite-difference time-domain method.

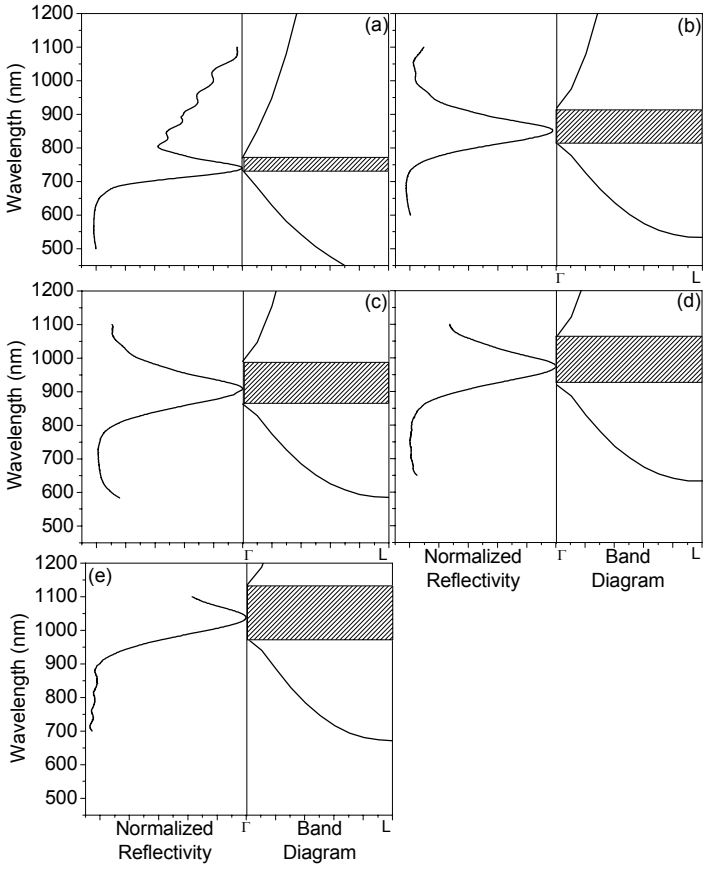

Fig. 12. Comparison of the calculated positions of the 2nd and 3rd photonic bands with reflectivity spectra for: (a) a 5.9% filling fraction TiO_2 NCP inverse opal and after backfilling with (b) 160 (c) 280 , (d) 400, and (e) 520 ALD cycles, respectively. For all calculations $n_{an} = 2.65$, $n_{am} = 2.45$. (15°)

Figure 13 shows the evolution of the higher order reflectivity spectra and photonic band features as a function of the conformal backfilling layer thickness. Prior to backfilling, the low filling fraction inverse opal exhibited high order peaks at 392 and 427 nm. It should be noted that the photonic band diagram calculations do not predict a PBG for this structure, but there is significant band flattening, that is attributed to the presence of these two reflectivity peaks. After backfilling the structure with 12 nm of TiO_2, the observed reflectivity structure was moved to significantly longer wavelengths, due to the increased dielectric material added to the structure, and showed well-defined peaks at 485, 430, and a feature at 533 nm. The calculated band diagram agrees very well with experiment and now correlates the reflectivity peaks with the existence of three PPBGs, as indicated by the shaded boxes in Figure 13(b). After backfilling with a further 6 nm of TiO_2, to a total thickness of 18 nm, the observed reflectivity and corresponding band diagram (Figure 13(c)) shows the same three PPBGs, but now the gaps, at slightly longer wavelengths of ~ 575 nm and 500 nm are predicted to widen, and the gap at ~440 nm to narrow. Again, the band structure prediction agrees extremely well with the reflectivity data that exhibits peaks at 450 nm, 518 nm, and a barely discernable peak at 577 nm. After 24 nm of backfilling the three PPBGs are

still predicted; the two "upper" gaps (now at ~ 543 and 608 nm) widened further, whereas the "lower" gap (~458 nm) is almost closed. These are in good agreement with the reflectivity data that exhibits peaks at 555 nm, and 608 nm, although the third (high energy peak) has disappeared. After 30 nm of ALD backfilling, Figure 13(e), the band diagrams now predict the existence of four PPBGs centered at 635, 569, 510, and 473 nm, whereas the reflectivity only shows one broad peak, with a maximum at 594 nm. This variation may be due to development of a layer on the milled surface that deviates from the topology within the NCP inverse opal, an effect that increases with high levels of backfilling.

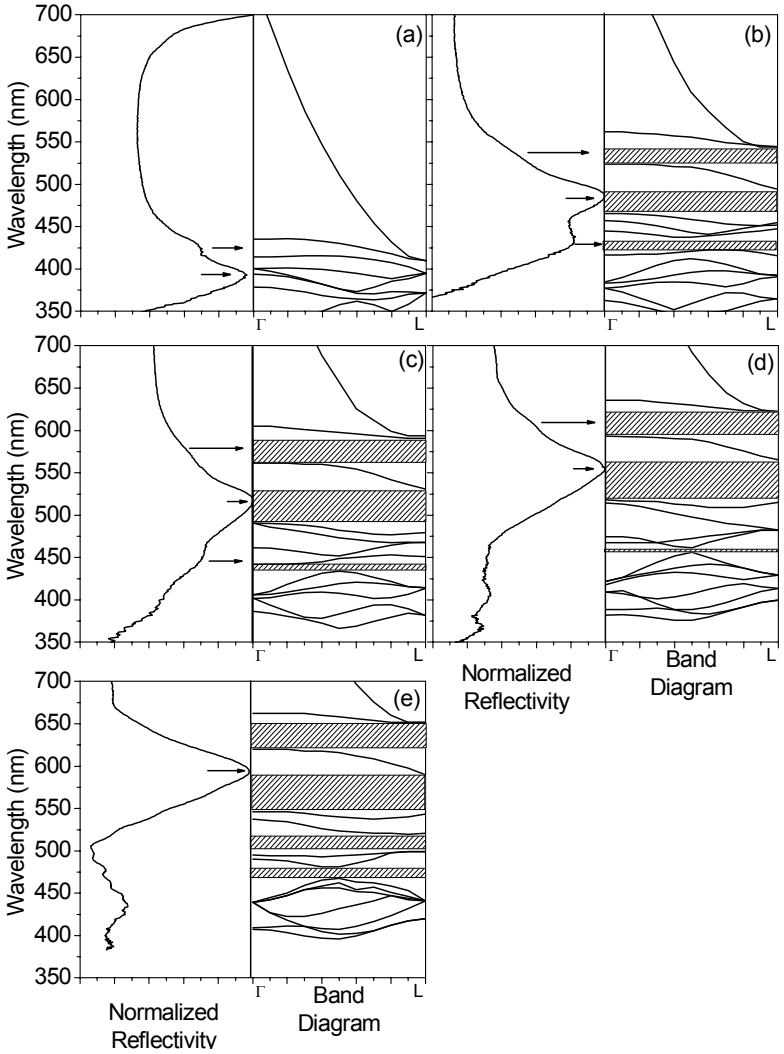

Fig. 13. Comparison between calculated photonic band diagrams and the higher order reflectivity spectra for: (a) NCP inverse opal (n_{an} = 2.95), and after (b) 12 nm (n_{an} = 2.75, n_{am} = 2.52), (c) 18 nm (n_{an} = 2.68, n_{am} = 2.47) (d) 24 nm (n_{an} = 2.6, n_{am} = 2.4) and (e) 30 nm (n_{an} = 2.56, n_{am} = 2.36) of conformal TiO_2 backfilling.

For example, in Figure 11, clearly the top (exterior) surface's features grow differently than the interior, with rounded ball-like features forming at the tetrahedral interstitial positions. Despite this slight deviation, throughout the drastic structural modification enabled by conformal backfilling of the modified inverse

opal template, both the fundamental and higher order reflectivity data show a high level of consistency and excellent agreement with theory. These measurements show excellent correspondence with the proposed model, supporting the geometrical evolution of the structure achievable by controlled sintering and ALD backfilling.

Figure 14 shows the dependence of the Bragg and higher order peak position on the number of ALD cycles. The data was taken from reflectivity data measured after every set of 40 ALD cycles. As shown in Figure 14, the Bragg (Γ-L) photonic band gap increases linearly with infiltration. Also, as discussed above and shown in the figure, two high order peaks were observed for 0 to 120 ALD cycles, three peaks between 120 to 320 cycles, and one peak from 320 to 520 cycles.

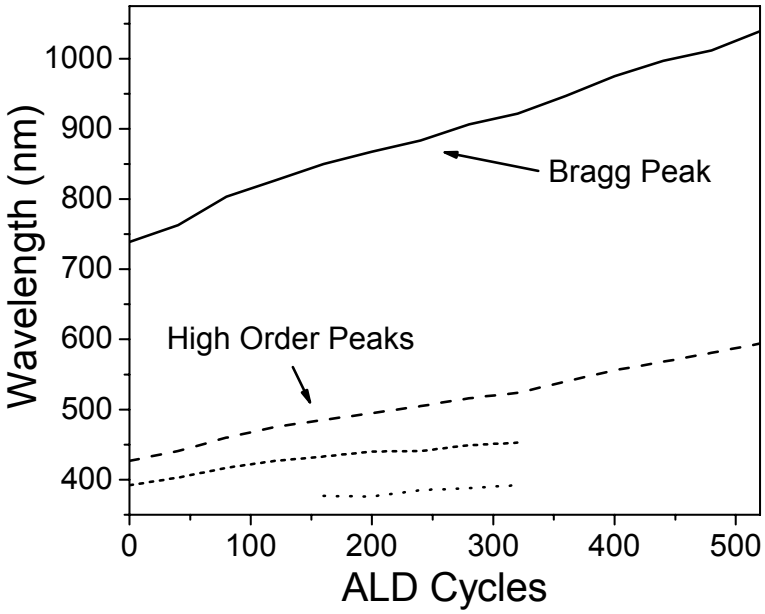

Fig. 14. Dependence of the Bragg peak position (solid line) and higher peak positions (dash, short dash, and dotted lines) on number of ALD cycles.

3. Conclusions

We have reported a comprehensive investigation of synthetic opals and inverse opals and shown that ALD is an effective infiltration method for fabricating inverse opal PCs. Over >95% infiltration of the pore volume was achieved for ZnS:Mn and TiO_2 and large PPBGs demonstrated in inverse ZnS:Mn, TiO_2 and multi-layered photonic crystals. Also composite luminescent and high index materials were formed. For all of these structures the photonic band theory data agreed very well with the reflectivity data. The strong PL modulation demonstrated in ZnS:Mn was well correlated with the reflectance data and presence of PPBGs. In addition, we reported several new schemes for enhancing the properties of opal-based structures that include techniques for making non-close-packed inverse opals and the backfilling of these structures to add measured thicknesses of dielectric material. These investigations dramatically demonstrate

the effectiveness of dielectric placement techniques in controlling optical properties and specifically, showed that by conformally backfilling these non-close-packed multi-layered PCs structures, it was possible to tune the reflectance by over twice the initial wavelength and to increase the bandwidth by approximately 50%. The combination of multi-layered growth of high refractive index and luminescent materials with these structures will provide new opportunities to control light. Additionally, because of their openness and high dielectric properties NCP opals provide the best opportunity to obtain tunable devices by the incorporation of liquid crystals into the inverse opal.

Thus, this study demonstrates a practical pathway to grow complex luminescent photonic crystal structures and optical microcavities. The extension of these techniques is expected to produce luminescent and dynamically tunable devices and to be directly applicable to the fabrication of lower symmetry 3D lithographically derived structures.

Acknowledgement

This work was supported by the U.S. Army Research Office under MURI contract DAAD19-01-1-0603.

References

[1] S. John, *Phys. Rev. Lett.* **58** (1987) 2486.

[2] E. Yablonovitch, *Phys. Rev. Lett.* **58** (1987) 2059.

[3] D. L. C. Chan, E. Lidorikis and J. D. Joannopoulos, *Phys. Rev. E* **71** (2005) 56602.

[4] G. Mertens, R. B. Wehrspohn, H.-S. Kitzerow, S. Matthias, C. Jamois and U. Gösele, *Appl. Phys. Lett.* **87** (2005) 241108.

[5] K. Busch and S. John, *Phys. Rev. E* **58** (1998) 3896.

[6] E. Yablonovitch, T. J. Gmitter and K. M. Leung, *Phys. Rev. Lett.* **67** (1991) 2295.

[7] M. Maldovan and E. L. Thomas, *Nature Mater.* **3**, 593 (2004).

[8] S. Y. Lin, J. G. Fleming, D. L. Hetherington, B. K. Smith, R. Biswas, K. M. Ho, M. M. Sigalas, W. Zubrzycki, S. R. Kurtz and J. Bur, *Nature* **394** (1998) 251.

[9] S. H. Park, D. Qin and Y. Xia, *Adv. Mater.* **10** (1998) 1028.

[10] A. Blanco, E. Chomski, S. Grabtchak, M. Ibisate, S. John, S. W. Leonard, C. Lopez, F. Meseguer, H. Miguez, J. P. Mondia, G. A. Ozin, O. Toader and H. M. van Driel, *Nature* **405** (2000) 437.

[11] Y. A. Vlasov, X.-Z. Bo, J. C. Sturm and D. J. Norris, *Nature* **414** (2001) 289.

[12] Y. Xia, B. Gates, and S. H. Park, *J. Lightwave Technol.* **17** (1999) 1956.

[13] J. S. King, C. W. Neff, C. J. Summers, W. Park, S. Blomquist, E. Forsythe and D. Morton, *Appl. Phys. Lett.* **83** (2003) 2566.

[14] J. S. King, C. W. Neff, S. Blomquist, E. Forsythe, D. Morton and C. J. Summers, *Phys. Stat. Sol. B* **241** (2004) 763.

[15] J. S. King, E. Graugnard and C. J. Summers, *Adv. Mater.* **17** (2005) 1010.

[16] D. Heineman, *M.S. Thesis,* Georgia Institute of Technology (2004).

[17] J. S. King, D. P. Gaillot, E. Graugnard and C. J. Summers, *Adv. Mater.* **18** (2006) 1063.

[18] D. P. Gaillot and C. J. Summers, *J. Appl. Phys.* (submitted).